ORIGINAL ARTICLE

Colloidal Quantum Dot Solid-Based Infrared Optoelectronics Enabled by Solution-Phase Ligand Exchange

Min-Jae Si[1] · Dongeon Kim[1] · Seoryeon Jeong[1] · Minjung Yang[1] · Jeongeun Kim[1] · Seo-Young Lee[1] · In-Suh Lee[1] · Jaewoo Jeong[1] · Byeong-Chan Kim[1] · Taeho Han[1] · Beomkwan Kim[1] · Yongnam Ahn[1] · Seungin Jee[1] · Yujin Jung[2] · Se-Woong Baek[1]

Abstract

This study explores the rational strategy to build lead sulfide (PbS)-based colloidal quantum dots (CQDs) solid for high performance photodetection and solar energy conversion in the near- and short-wave infrared spectra. We demonstrated a facile engineering process from CQD synthesis to infrared CQD devices fabrication. By controlling the monomer concentration, we effectively tuned the infrared absorption characteristics and the solution-phase surface ligand exchange resulted in highly concentrated CQD ink, facilitating the formation of uniform, and thick CQD solids, which is crucial for high absorption efficiency. The CQD-based infrared photodetector achieved a specific detectivity of approximately 10^{11} Jones and fast response times under 100 ns. Furthermore, optimized PbS CQDs were utilized in solar cells and achieved high quantum efficiency across visible to infrared spectrum, indicating a significant potential for 2-terminal tandem structures with perovskite front cells.

Min-Jae Si, Dongeon Kim, and Seoryeon Jeong contributed equally to this work.

✉ Yujin Jung
yj_jung@yu.ac.kr

✉ Se-Woong Baek
sewoongbaek@korea.ac.kr

Min-Jae Si
tlalswo96@naver.com

Dongeon Kim
kdu918@korea.ac.kr

Seoryeon Jeong
98cristy@naver.com

Minjung Yang
mjy1495@gmail.com

Jeongeun Kim
kim0994@korea.ac.kr

Seo-Young Lee
seyong103@gmail.com

In-Suh Lee
lis1895@korea.ac.kr

Jaewoo Jeong
splender84@korea.ac.kr

Byeong-Chan Kim
grape000206@gmail.com

Taeho Han
tony11382@gmail.com

Beomkwan Kim
kenkim943@gmail.com

Yongnam Ahn
yongnam123@korea.ac.kr

Seungin Jee
tmddls1133@korea.ac.kr

[1] Department of Chemical and Biological Engineering, Korea University, Seoul 02841, Republic of Korea

[2] School of Chemical Engineering, Yeungnam University, 280 Daehak-ro, Gyeongsan, Gyeongbuk 38541, Republic of Korea

Introduction

Colloidal quantum dots (CQDs) are semiconductor nanocrystals that enable to adjust optical bandgap through the quantum confinement effect, which is a significant advantage to broadband optoelectronics [1–6]. Specifically, lead sulfide (PbS)-based CQD can tune the broadband absorption across visible to infrared spectrums and exhibits high absorption coefficient ($> 10^4$ cm^{-1}) [7, 8]. Therefore, PbS CQD is one of the representative materials that are widely used in various applications such as photodetectors [9–11], solar cells [12–16], and photocatalysts [17, 18].

Extensive research has been reported on PbS CQDs, particularly in the NIR-SWIR range of 1100–1800 nm, which silicon does not absorb. Infrared photodetector, especially beyond 1400 nm wavelength, are important because of eye-safety issue and 1550 nm wavelength exhibits low atmospheric scattering, serving as a central role in long-distance communications such as autonomous driving and various smart system [19]. Recently, PbS CQD-based photodiode showed an external quantum efficiency (EQE) of over 80% and response times below 10 ns, proving the potential to SWIR photodetector [20].

Furthermore, solar radiation energy harvesting beyond the silicon absorption band (> 1100 nm) can generate approximately 15 mA/cm^2 of photocurrent, and theoretically, an additional power conversion efficiency (PCE) of 8% can be achieved, which is significant [21–23]. Therefore, various studies have demonstrated solar cells that absorb in a range of 1100–1800 nm [24–26]. PbS CQDs have been proposed as one of the most promising alternatives to traditional bottom cell materials for triple-junctions, such as InGaAs or Ge. Recent advances in PbS CQD solar cells achieved an EQE of ~80% at 1750 nm and collected infrared photocurrent of 10 mA/cm^2, which is 60–70% of incident infrared irradiation [27].

However, though several promising strategies are reported as discussed above, general process engineering, from CQD synthesis to infrared device fabrication, is not fully suggested. This research presents a facile engineering process capable of fabricating high-performance infrared PbS CQD devices. We demonstrated how to simply adjust the infrared absorption characteristics by controlling CQD sizes. Furthermore, solution-phase surface ligand exchange enables the production of highly concentrated CQD ink, which can be utilized to form a uniform CQD solid. Specifically, the dynamic coating process allows for sufficiently thick CQD solids, securing high absorption efficiency, which is significantly important for infrared devices.

Eventually, using thick CQD solid, we fabricated and evaluated infrared photodetectors and solar cells. We performed various measurements to understand how surface ligand control affects the performance of the photodetector and achieved a specific detectivity of approximately 10^{11} Jones and response times below 100 ns. Furthermore, the optimized CQD was also applied to infrared solar cells. Particularly, we studied the best bandgap options to match current with the perovskite front cells for a potential 2-terminal tandem structure and finally rendered a solar cell with excellent quantum efficiency across the entire absorption range.

Results and Discussions

Utilization of Solar and Electromagnetic Spectrum

As shown in the electromagnetic spectrum, specific absorption bands are required to realize various infrared applications (Fig. 1a). Specifically, for solar cells, high photocurrent is an important factor for high power conversion efficiency (PCE), implying that collecting the broadband solar irradiation is crucial. Perovskites solar cells typically absorb up to 800–850 nm, which can generate a photocurrent of 20–25 mA/cm^2, and silicon solar cells absorb up to 1100 nm, indicating that *approx.* a photocurrent of 40 mA/cm^2 can be generated. (Fig. 1b) Since approximately 15 mA/cm^2 of photocurrent is still able to be harvested beyond silicon, which is a significant value, a device that can effectively absorb from 1100 to 1800 nm range is required to fully utilize solar irradiation.

Meanwhile, for infrared imaging, the important bands are determined depending on the application areas. For example, the in vivo bioimaging field requires the 1000–2000 nm bands, and material classification for environment requires the 1100–1700 nm bands [28, 29]. Therefore, infrared photodetectors are mainly operated for ranging and object recognition. Typical silicon photodetectors in the 905–940 nm bands were used in previous, but considering the eye-safety, sensing beyond 1400 nm is important. Especially, the wavelength of 1550 nm has low atmospheric scattering, allowing it to be utilized in long-range communication and energy transmission systems [30]. For thermal sensors, the spectrum blue-shifts as the temperature of the heat source increases, according to Planck's blackbody radiation. Therefore, a smaller bandgap is advantageous for sensing a wide range of temperatures [24]. In conclusion, to utilize various infrared fields as described above, controlling the bandgap is crucial, and thus, CQDs hold potential as the next generation of infrared materials.

Fig. 1 The application of IR optoelectronics. **a** Solar spectrum (red) and accumulated current density (yellow). **b** Various applications in IR range. The grey area depicts the IR wavelength range which can extract extra current beyond c-Si
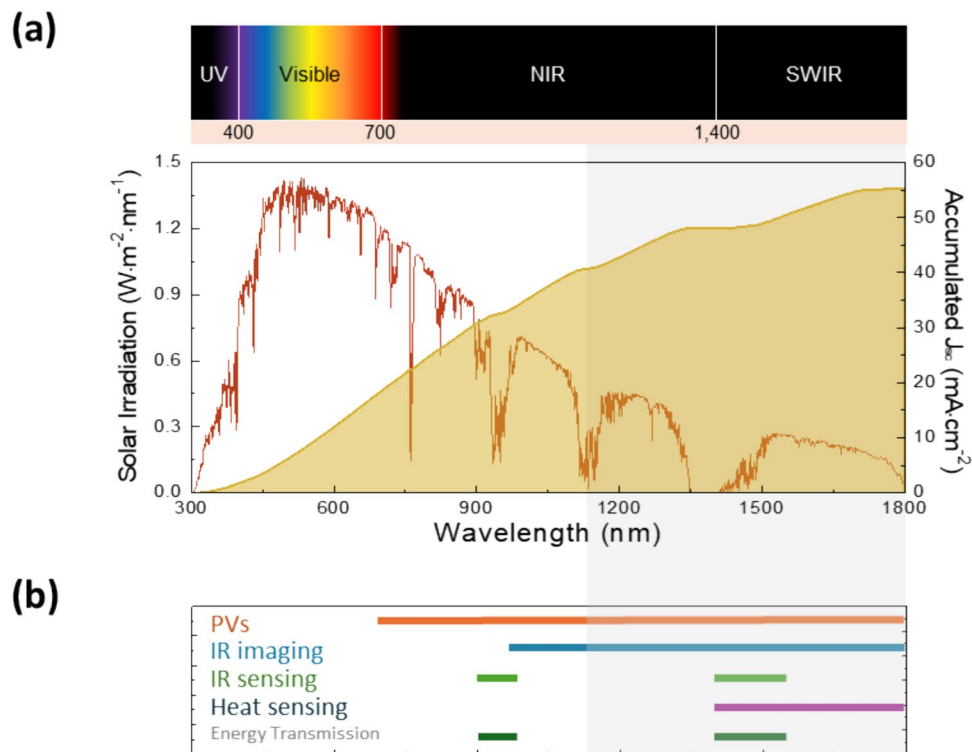

Facile Strategy to Adjust Bandgap of PbS CQD

For the synthesis of PbS CQD, the hot injection using Pb(OA)$_2$ and (TMS)$_2$S as reaction precursors is one of the widely used methods [31, 32]. The size of the nanocrystals can be controlled by the amounts of precursors, concentration of ligand, growth time, and temperature [33–36]. Among various conditions, we tuned the size of the OA-capped PbS CQDs by controlling the concentration of oleic acid (OA). The amount of PbO and 1-octadecene to form lead oleate and the injection temperature were fixed and the synthesis was carried out by varying the amount of OA. In the case of the injection temperature, the higher temperature of 110 °C was fixed to synthesize larger quantum dots compared to small-size CQD (892 nm at 94 °C) by accelerating precursor diffusion, resulting in faster growth [37]. The first excitonic peak of PbS QDs shifts to the longer wavelength band as the amount of OA increases, as shown in Fig. 2a. During the CQD synthesis, the monomers are consumed, resulting in nucleation and QD growth. As the monomer solubility is increased by free acid during synthesis, additional monomers are consumed for QD growth rather than nucleation, resulting in larger QDs [38, 39]. Therefore, it can be explained that the monomer solubility increased with the increase of oleic acid, resulting in a larger QD. As a result, the first excitonic peak at 1531 nm was obtained for 35.754 ml of OA. Transmission electron microscopy (TEM) images of the PbS CQDs with first excitonic peaks

at 892, 1097, 1307, and 1531 nm were obtained to compare the sizes of the CQDs (Fig. 2b, c). The average size of each sample was measured to be 3.27 ± 0.10, 3.51 ± 0.011, 4.32 ± 0.11 nm, and 5.2 ± 0.11 nm. The red-shift of the 1st excitonic peak was observed as the size increased. Full-width at half-maximum (FWHM) and peak to valley ratio (p/v) are obtained from absorbance spectra (Fig. 2d, e). Smaller PbS CQDs exhibit FWHMs above 170 nm and p/v below 2.5, and the largest CQDs at 1531 nm exhibit the narrowest size distribution with a FWHM of 117 nm and p/v of 4.58. For 1531 nm CQDs, the mass-transfer coefficient decreases due to the high viscosity of the growth environment [40]. Therefore, the reactants are not efficiently transported to the surface of the nanoparticles, which limits their diffusion to the surface and converts the growth process into a diffusion-controlled growth regime. This contributes to the size-focusing of the colloidal quantum dots [41]. The FWHM of PbS CQDs with similar absorption bands synthesized in previous studies ranges from 110 to 200 nm, indicating that synthesized PbS CQDs are uniform [42, 43]. As a result, this synthesis is a facile method to tune to IR CQD from 900 to 1600 nm because bandgap control is demonstrated by only controlling the OA concentration.

PbS CQD-Based Infrared Optoelectronics

PbS CQDs synthesized as described above have long organic ligands bound to the surface after synthesis for the purpose
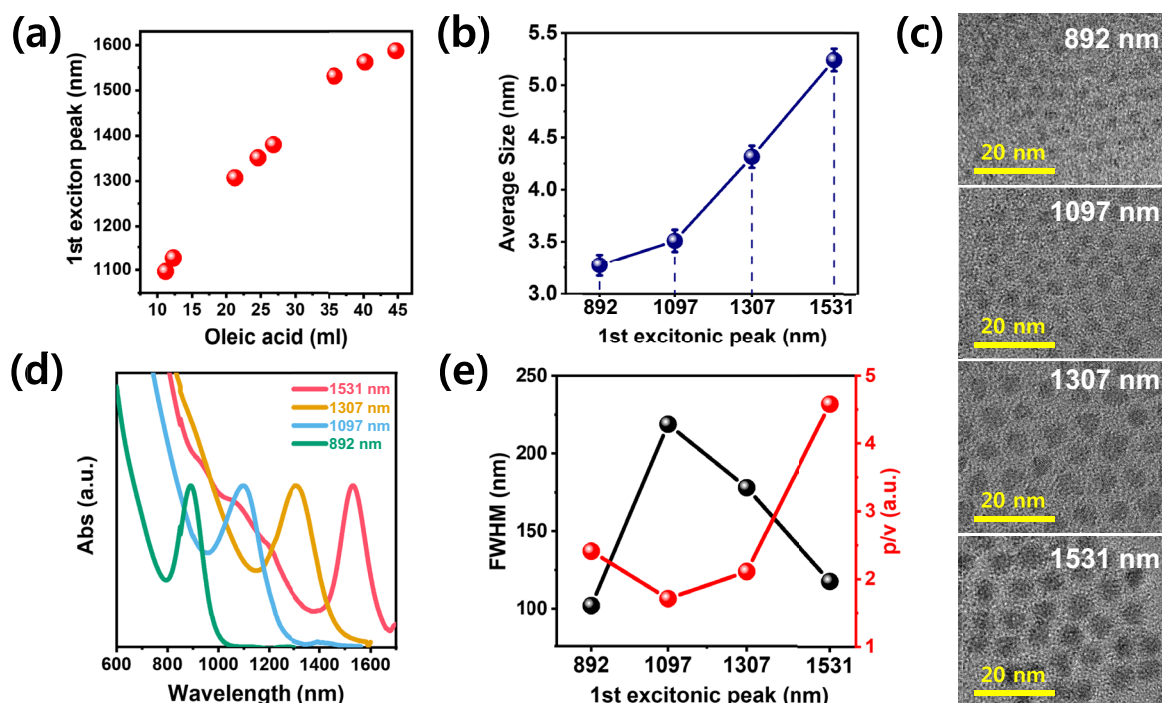
Fig. 2 PbS CQDs synthesis. **a** 1st excitonic peak of PbS CQDs according to the amount of oleic acid used in synthesis. The lead(II) oxide used to make lead oleate was fixed at 0.9 g and 1-octadecene at 33.349 ml. **b** Average size and **c** TEM images of PbS CQDs of various 1st excitonic peaks. **d** Absorbance spectra were measured in solu-tion dispersed in octane: 1st excitonic peak 1531 nm (red), 1307 nm (yellow), 1097 nm (blue), and 892 nm (green), respectively. **e** The FWHM (black) and peak to valley ratio (*p/v*) (red) analyzed from absorption spectra

of high colloidal stability in the solution phase and passiva-tion of surface dangling bonds [44]. However, the ligands based on long alkyl chains hinder charge transfer in the CQD solids; therefore, the short ligands should be utilized

to facilitate charge transfer between the CQDs [24]. We uti-lized a ligand exchange method, the solution-phase ligand exchange (SPLE) method (Fig. 3) [45]. During the SPLE process, as-synthesized CQDs with long-chain ligands are
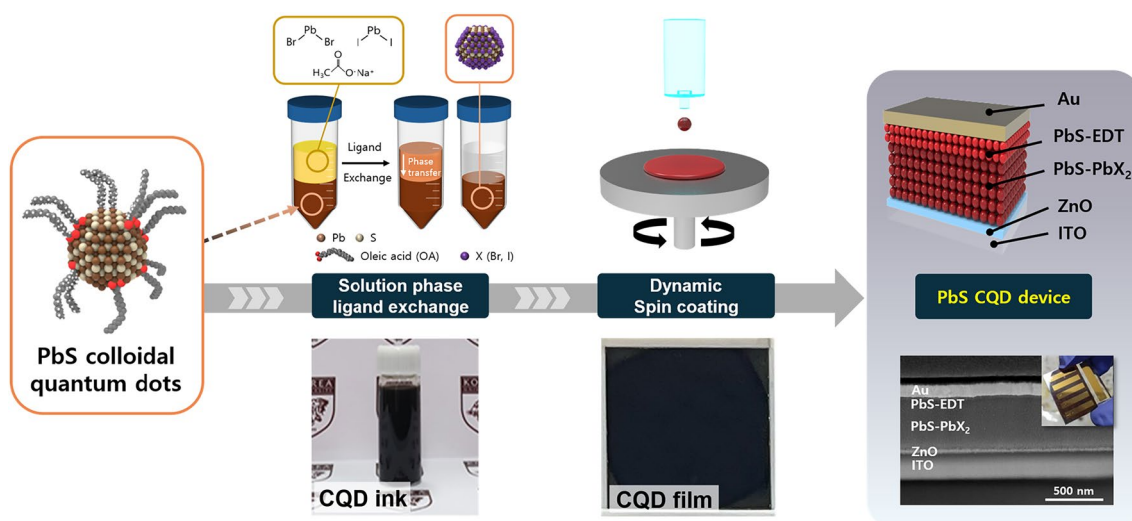
Fig. 3 Schematic of the fabrication of PbS CQD-based devices through ink fabrication by solution phase ligand exchange of PbS CQDs and film fabrication by spin coating process

dispersed in a non-polar solvent (i.e. octane). We mixed a CQD solution with a ligand precursor, short hydrophilic molecule-based ligands, PbX_2 (X: Br, I), dissolved in a polar solvent. The precursor solution detaches the long alkyl chain ligands and attaches the short ligands at CQD surface through a phase transfer process [46]. We then employed the dynamic spin coating process, dropping of CQD ink during the rotation of the substrate, to achieve thick and uniform CQD thin-films to increase light absorption [25]. SPLE minimizes partial ligand loss by the protic solvent effect that occurs in conventional solid-state ligand exchange at the CQD surface and enables a lower film fabrication time [47]. The dynamic spin coating process involved the initial spinning of the substrate and the subsequent deposition of the CQD ink at the desired speed. The substrate was then rotated at a faster speed to remove the residual solvent. The process enables the formation of a uniform CQD film while the substrate rotates at a slower speed, which increases the thickness of the CQD thin film and improves the wettability of the film [48]. Empirically, CQD-based films using the dynamic spin-coating method exhibit a more uniform morphology and increased thickness compared to those made with the control spin-coating method (Fig. 4a). These improved film properties further enhanced the dark *I–V* characteristics, resulting in lower dark current and higher shunt resistance (Fig. 4b). Finally, we fabricated the device using an ITO/ZnO/PbS–PbX_2/PbS–EDT/Au architecture, with a PbS–PbX_2 layer as the active layer and PbS–EDT and ZnO sol–gel as the hole and electron transport layers, respectively.

PbS CQD-Based Infrared Photodetector

We confirmed the rectifying behavior of the CQD-based photodiode by analyzing the dark current characteristics as a function of voltage (Fig. 5a). We changed the surface passivation method of CQDs to achieve the optimal photodiode characteristics of the CQD-based devices. To this end, we increased the concentration of $PbBr_2$ from 0.02 to 0.04 M in the PbX_2 ligand precursor solution and characterized the devices. We compared the dark current densities of the two conditions and showed a higher rectification ratio (dark current at + 1 V/dark current at − 1 V) [49] of 909.7 at a higher concentration of $PbBr_2$ than 27.6 in the control group (0.02 M), indicating an improvement in rectification characteristics of about 33 times. We attributed the disparity in performance to the difference in CQD surface passivation caused by the change in ligand precursor concentration [50] (Table 1).

As the CQDs are larger than 4 nm, the ratio of charge-neutral (100) facets to Pb-rich (111) facets gradually increases, which decreases the efficiency of surface passivation by the PbI_2 ligands [51]. $PbBr_2$, which is smaller than PbI_2, is known to have a relatively higher affinity for the (100) facets [52]. Increasing the concentration of $PbBr_2$ in a mixture of lead halides enables more efficient surface coverage. An effectively passivated CQD surface can prevent unnecessary CQD fusion caused by unprotected (100) facets in the solution phase, resulting in a uniform thin film, and can improve the charge transfer within the thin film [20]. In addition, we expect that the leakage current at reverse voltage was reduced by the suppressed defects caused by surface passivation, which is the origin of enhancing the rectifying behavior [53].

We further characterized the responsivity to analyze the optoelectronic properties of the surface-modified PbS CQD-based devices (Fig. 5b). The responsivity was calculated from the external quantum efficiency (EQE) measured at 0 V and − 2 V using the following equation (Eq. (1)) [54]:
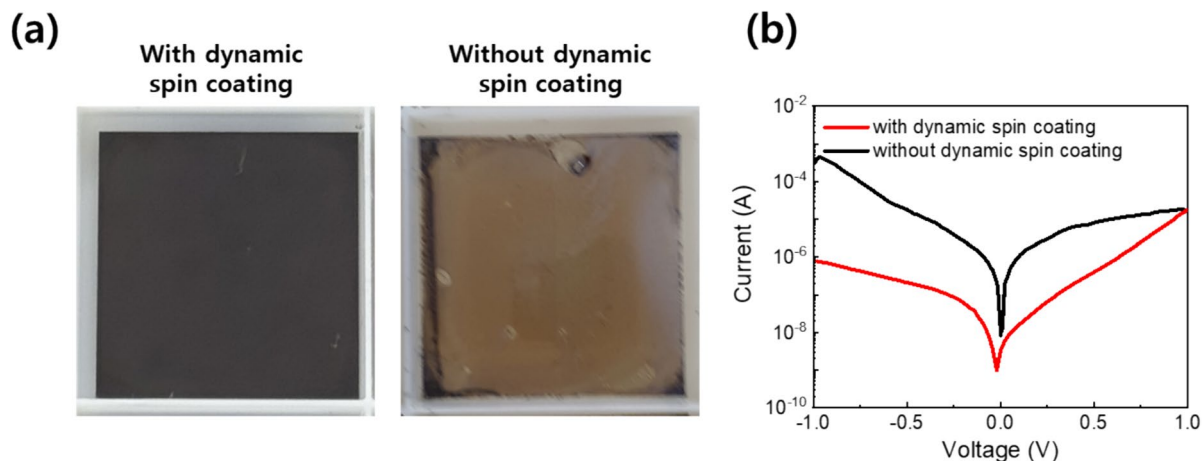
Fig. 4 Result of dynamic spin-coating method on CQD-based devices. **a** Photographs of CQD thin films fabricated with (left) and without (right) dynamic spin-coating. **b** Dark *I–V* curves of CQD-based photodiodes with (red) and without (black) dynamic spin-coating
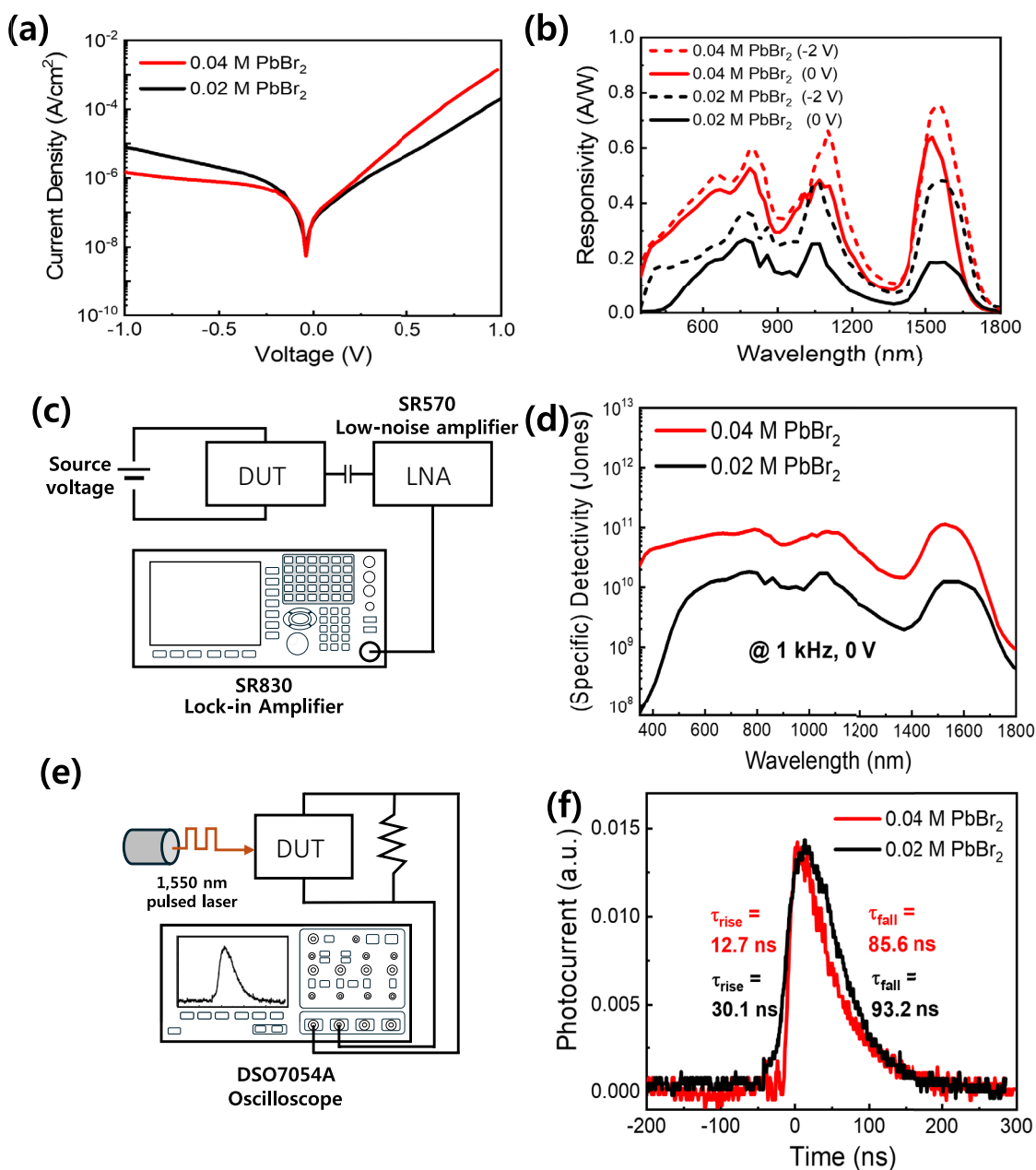
Fig. 5 PbS CQD-based infrared photodiode. **a** Dark current density of PbS CQD-based photodiode with 0.04 M concentration of Br (red) compared to the control photodiode (black). **b** Responsivity spectra of PbS CQD-based photodiode with high concentration of Br (red) compared to the control photodiode (black) under 0 V (line) and −2 V bias (dashed). **c** Schematic illustration of measurement setup to configure noise figure of a device-under-test (DUT). **d** Specific detectivity spectra of PbS CQD-based photodiode with high concentration of Br (red) compared to the control photodiode (black) under zero-biased condition. The specific detectivity is calculated based on responsivity and noise equivalent power (NEP) measured at 1 kHz frequency. **e** Schematic illustration of measurement setup to configure time-dependent photoresponse of a DUT. **f** Time-dependent photoresponse of PbS CQD-based photodiode with 0.04 M concentration of Br (red) compared to the control photodiode (black) without external applied bias. The photoresponse was measured under pulsed illumination of 1550 nm light (1 mW, 10 ns pulse width)

Table 1 PbS 1550 nm photodetector performance table under 0 V and 1 kHz frequency

	Responsivity (A/V)	NEP (W/Hz$^{-1/2}$)	(Specific) Detectivity (Jones)	Rise/fall time (ns)
0.04 M PbBr$_2$ conc.	0.63 (0.78[a])	2.567×10^{-12}	1.134×10^{-11}	12.7/85.6
0.02 M PbBr$_2$ conc.	0.18 (0.48[a])	2.530×10^{-11}	1.249×10^{-10}	30.1/93.2

[a]Responsivity measured with applied reveres bias (−2 V)

$$R = \text{EQE} \times \frac{\lambda}{1240}. \tag{1}$$

The device with 0.04 M PbBr$_2$ exhibited 0.63 A/W at 0 V compared to 0.18 A/W with 0.02 M PbBr$_2$, which is 3.5 times improved performance. The responsivity under the reverse bias (− 2 V) was obtained as 0.78 A/W and 0.48 A/W, respectively. The performance improvement of devices with 0.04 M bromide originates from the improved CQD surface passivation [55].

We tested the noise characteristics of PbS CQD-based photodiodes to directly analyze their photodetector performance based on their optoelectronic properties. The noise characteristics were measured by connecting the SR570 low-noise amplifier (LNA), which can amplify RF noise to a certain ratio, and the SR830 lock-in amplifier, which can extract the noise signal synchronized with the frequency (Fig. 5c). The noise figure of the device-under-test (DUT) was measured at a frequency of 1 kHz under dark conditions. The noise current (A/Hz$^{-1/2}$) was calculated by multiplying the noise voltage (V/Hz$^{-1/2}$) readout of the lock-in amplifier by the sensitivity (A/V) of the LNA [56]. The device treated with 0.04 M PbBr$_2$ exhibited a noise level of 1.617×10^{-12} A/Hz$^{-1/2}$, which was approximately 64.5% lower than that of the control device (4.554×10^{-12} A/Hz$^{-1/2}$) (Table 1). The lower noise level of the device with 0.04 M PbBr$_2$ is probably affected by a reduction in thermal and shot noise, resulting from a decrease in the dark current [57].

We characterized the (specific) detectivity (D^*) using the responsivity and noise current (Fig. 5d). The detectivity was calculated using the following equation (Eq. (2)) [2]:

$$D^*(\text{specific detectivity}) = \frac{R\sqrt{A}}{\text{noise current}}(A : \text{ device area}). \tag{2}$$

The device with 0.04 M of PbBr$_2$ concentration showed 1.134×10^{11} Jones at 1550 nm under 0 V and 1 kHz conditions, which is approximately 9 times higher than the 1.249×10^{10} Jones of the control group.

We further examined the transient photoresponse of CQD-based photodiodes to obtain device speed. The time-dependent photoresponse was measured through an oscilloscope using a 1550 nm pulsed laser (1 mW, 10 ns pulse width) at 0 V (Fig. 4e and f). Rise/fall time was characterized by measuring the time interval between 10 and 90% of the rise signal and the time interval between 90 and 10% of the decay signal, respectively. The fall time of the devices with 0.04 M PbBr$_2$ showed 10% faster decay of 85.6 ns compared to the control group. The faster response of the devices is presumably because of the decrease in the number of surface traps, which lowered the capacitance and improved charge transfer [7].

PbS CQD Solid for Infrared Solar Cell

The bandgap of light-absorbing material determines the theoretical efficiency limit of a solar cell. A light-absorbing material absorbs higher-energy photons than the material bandgap and produces photogenerated current and photovoltage. According to the Shockley–Queisser single junction solar cell limitation, as the bandgap decreases, there is a trade-off between photocurrent and photovoltage, resulting in a theoretical maximum efficiency of 33.16% for an optimum bandgap of 1.34 eV [58–60]. Multijunction solar cells are gaining interest in overcoming the theoretical efficiency limit. Multijunction solar cells utilize light-absorbing layers with different bandgaps to reduce thermalization and optical loss. Due to the limited infrared absorption range of silicon up to 1100 nm, low-bandgap light-absorbing materials such as InGaAs (~ 0.8 eV) and Ge (~ 0.67 eV) have mostly been used. However, their high cost restricts their commercial viability. Therefore, PbS CQD solar can be one of the attractive strategies to utilize in low-cost solution processes for infrared CQD solar cells.

Perovskite is a low-cost, solution-processed, suitable bandgap light-absorbing material that is promising today as a high-efficiency single- and multi-junction solar cell material. Designing a high-bandgap perovskite solar cell as the top cell and a low-bandgap CQD solar cell as the bottom cell, as shown in Fig. 6a, can theoretically yield a 43% efficiency if the CQD bottom cell absorbs the infrared light that perovskite cannot absorb [61]. The open-circuit voltage (V_{oc}) of a 2-terminal solar cell is the sum of the top and bottom cell V_{oc}, and the short-circuit current density (J_{sc}) is limited by the lower J_{sc} cell, implying that a current-matching is required to minimize efficiency losses in a tandem solar cell.

CQD can change its absorption range depending on its size; at the same time, perovskite can also change its absorption range by adjusting its bandgap depending on the composition of the material (Fig. 6b). Therefore, for
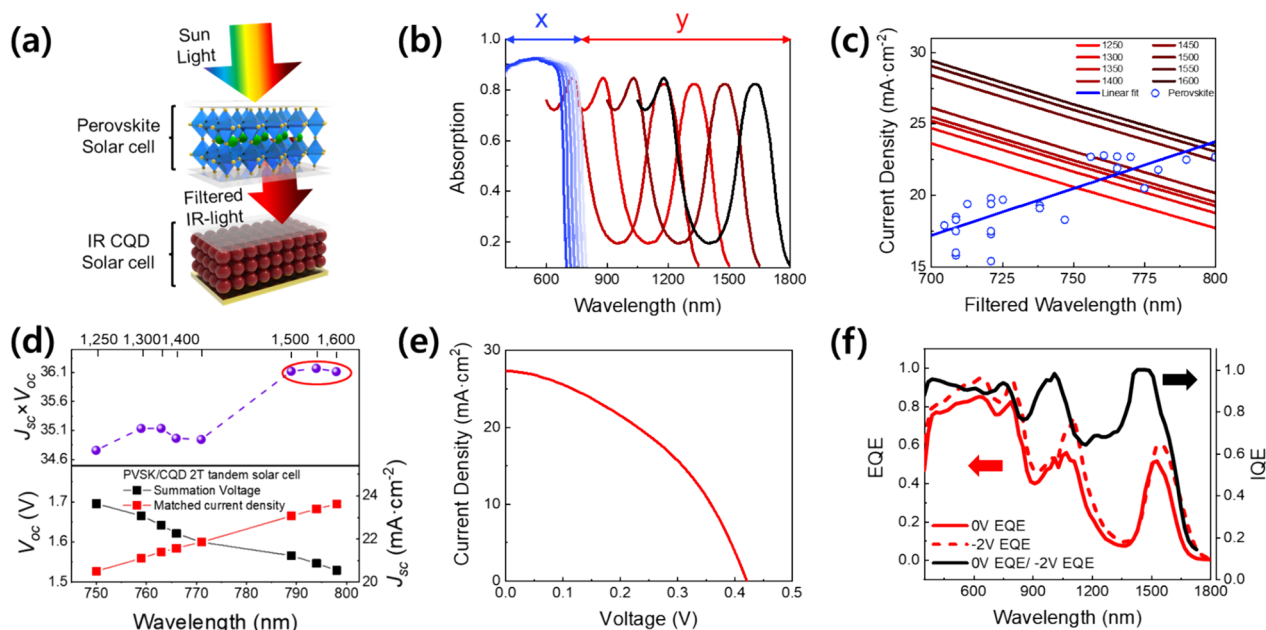
Fig. 6 PbS CQD infrared solar cell. **a** Schematic of perovskite/IR CQD tandem solar cell. IR CQD bottom cell can convert IR light and add additional efficiency to perovskite front cell. **b** Absorption of perovskite(blue) and IR CQD (red) with different bandgap, x is absorption range of perovskite, y is absorption range of IR CQD. **c** Short-circuit current density of PbS CQD solar cells with different wavelength filters and band gaps. The color gradually changed from red (1200 nm) to black (1600 nm) as the band gap of the PbS

CQD. The blue scatters and line represent the short-circuit current of the perovskite solar cells according to the reported bandgaps, and its linear fit. **d** Current matching J_{sc} (red square) and summation of V_{oc} (black square) of perovskite and IR CQD solar cells corresponding to the current matching bandgap pairs. The product of J_{sc} and V_{oc} (purple circle) of perovskite and CQD solar cell. **e** The J–V curve of PbS 1550 nm solar cell (red, solid). **f** EQE (0 V, black, solid), EQE (−2 V, red, dash), and IQE (black, solid) curves of PbS 1550 nm solar cell

optimal efficiency of CQD and perovskite tandem solar cells, it is important to find the optimal bandgap pair for both CQD and perovskite to match current. To this end, we calculated the bandgap-dependent current density of the infrared CQD sub-cell through optical simulations based on the transfer matrix method (Fig. 6c). To calculate the theoretical current density of the sub-cell, we assumed the bandgap of the perovskite top cell. Our assumption is that photon with an energy smaller than the assumed perovskite bandgap would be transmitted, and photon with an energy larger than the assumed bandgap would not be transmitted. We calculated the J_{sc} of the CQD sub-cell by calculating the light absorption of the PbS large dot layer in the ITO/ZnO (30 nm)/PbS large dot (500 nm)/P-type PbS (40 nm)/Au (100 nm) structure by considering that the absorbed light comes out as a photocurrent. As a result, the photocurrent increased by more than 5.8 mA/cm^2 by increasing the absorption range of CQDs with a bandgap of 1250 nm (red) to 1600 nm (black).

We derived a linear regression of the current density against the perovskite bandgap to find a perovskite solar cell bandgap that is matched with the CQD sub-cell [62]. From the intersection of both straight lines, we were able to obtain CQD-perovskite optimal bandgap pairs. From the 1250 nm to the 1600 nm CQD, the J_{sc} increased from 20.5

to 23.6 mA/cm^2, and the paired perovskite absorption range is supposed be increased from 750 to 798 nm.

Based on the previous reports, we calculated the voltage sum from two sub cells to find the highest-efficiency bandgap pairs (Fig. 6d) [63, 64]. As the bandgap of the perovskite used as the top cell became smaller, the bandgap of the infrared CQD also became smaller, reducing the sum of the V_{oc}. In contrast, the J_{sc} tended to increase as the perovskite bandgap decreased. By multiplying the V_{oc} and J_{sc}, the efficiency limit ($J_{sc} \times V_{oc}$) and optimal bandgap pair of perovskites and infrared CQD for 2-terminal tandem solar cells were obtained. The effect of increasing the short-circuit current density was more dominant than decreasing the open voltage, and the optimal bandgap pair was identified at 794 and 1550 nm for perovskite and CQD, respectively. At the optimum bandgap pair, the attainable efficiency limit surpasses 36.1%.

We demonstrated infrared solar cells and analyzed the performances corresponding to the optimal bandgap, as shown in Fig. 6e. The solar cell achieved a J_{sc} of 27.4 mA/cm^2, a V_{oc} of 0.42 V, and a fill factor (FF) of 41.7%, resulting in a PCE of 4.80%. The solar cell had an excellent external quantum efficiency (EQE) of 48% at 1550 nm. We tested the EQE at a negative voltage of −2 V to understand the origin of high EQE. Under negative voltage conditions, the

CQD layer is completely depleted, allowing us to extract close to 100% of the charge; therefore, EQE at negative bias estimates the absorption of the device. We also estimate the internal quantum efficiency (IQE) by dividing the EQE by the light absorption (EQE under − 2 V) [65]. The calculation shows that the IQE is 87%, indicating that the high EQE originates from the high IQE. The high IQE is attributed to high-quality IR CQD solid due to the monodisperse IR CQD and efficient surface passivation strategy.

Conclusions

In this study, we suggested a rational strategy for fabricating efficient infrared optoelectronic devices based on CQDs from size-tunable CQD synthesis to device fabrication. We easily tuned the bandgap of CQD by adjusting the OA concentration from 892 to 1531 nm and following ligand exchange strategy using halides enables to form high quality CQD solids. Specifically, the higher concentration of the $PbBr_2$ ligands, which have a higher affinity for the (100) facets, led to efficient passivation, resulting in superior performance of CQD devices. Finally, infrared photodetector and solar cells are demonstrated, respectively. In particular, we studied the optimum configurations with perovskite front cell for 2-T tandem solar cells and found a promising result that the perovskite-1550 nm PbS CQD 2-T tandem solar cell has a potential to achieve over 36% PCE, showcasing that the further studies on CQD synthesis, ligand exchange, and device fabrication will lead to the next generation infrared optoelectronics.

Methods

PbS CQDs Synthesis

Materials

Lead(II) oxide (Puratronic, 99.999% metals basis), 1-Octadecene (Sigma–Aldrich, tech. 90%), oleic acid (Sigma–Aldrich tech. 90%), hexamethyldisilathiane (Sigma–Aldrich, synthesis grade), hexane (Sigma–Aldrich, ≥ 97.0% (GC)), ethyl alcohol (Duksan, 99.9% (HPLC)), n-octane ((Alfa Aesar, 98 + %), acetone (Daejung, 99.8%), toluene (Sigma–Aldrich, 99.9%).

Synthesis of PbS CQDs

Lead(II) oxide 0.9 g, 1-octadecene 33.349 mL, and oleic 10–45 mL were put into a 250 mL three-neck flask and degassed under vacuum at 110 °C. The injection solution was prepared by mixing 1-octadecene 2 mL, and hexamethyldisilathiane ((TMS)$_2$S) 0.420 mL. After degassing for 3 h, the air within the 3-neck flask was replaced with argon. After removing the heating mantle from the flask and during cooling, when the temperature reached 95 °C, the injection solution was rapidly injected. Following the removal of the heating mantle and during cooling, the injection solution was rapidly injected into the flask when the temperature reached 95 °C. As the solution cooled to 30 °C, the CQD solution was washed twice with hexane and ethyl alcohol. After the CQD solution had been dried in a vacuum oven for 6 h, it was dispersed in n-octane and filtered through a 20-µm PTFE filter.

The synthesis of small PbS CQDs targeting the 900 nm excitonic peak was carried out using 1.8 g of lead(II) oxide, 80 mL of 1-octadecene, and 7 mL of oleic acid. After degassing at 94 °C for 12 h, the mixture was cooled under an argon environment to 67 °C, followed by rapid injection of the prepared injection solution. The injection solution comprised a mixture of 1-octadecene 2 mL and (TMS)$_2$S 0.85 mL of. Upon reaching 30 °C, purification was conducted using acetone and toluene. Subsequently, the sample was dried in a vacuum oven for 6 h, dispersed in n-octane, and filtered.

PbS CQD Characterization

Transmission electron microscopy (TEM) images were obtained using a JEM-2100F model from JEOL LTD (Japan). For TEM sampling, the PbS solution was diluted in hexane. Samples were then made by applying 2–3 drops to a carbon grid. The absorption spectrum of the PbS CQDs solution was measured using the V-700 Series UV–VIS/NIR Spectrophotometer (Jasco). 20 µL of PbS CQDs dispersed in n-octane were redispersed in 3 mL of tetrachloroethylene (TCE) (Sigma–Aldrich, ≥ 99.5%) for measurement.

Device Fabrication

Cleaned indium tin oxide (ITO) glass substrates (30 Ω/square) were utilized as conductive substrates. For the electron transport layer, a ZnO sol–gel solution was prepared by mixing 1 g of zinc acetate dihydrate (99.999%, Sigma-Aldrich) and 0.28 wt% of ethanolamine (99.5%, Sigma-Aldrich) in 2-methoxyethanol (99.8%, Sigma-Aldrich) with a concentration of 260 mM, and the solution was stirred overnight. The ZnO sol–gel solution was then spin-coated at 3,000 rpm on a UV-ozone treated substrate and annealed at 200 °C for 30 min with controlled humidity. The as-prepared CQD ink was dynamically spin-coated at 800 rpm on the ZnO layer under N_2 conditions and accelerated to 2000 rpm. CQD-coated thin films were annealed in a N_2 condition at 70 °C for 15 min. For the hole transport layer, using the smaller synthesized PbS CQDs, two layers of

1,2-ethanedithiol (EDT)-treated CQDs were deposited on top of the PbS–PbX$_2$ layer through the layer-by-layer (LBL) process. In each layer, as-synthesized CQDs (50 mg/mL) were deposited, followed by a 30 s soaking in EDT solution (0.01 vol% in acetonitrile) and three times of washing with acetonitrile. Finally, 100 nm of gold was deposited as a top contact.

External Quantum Efficiency (EQE) Characterization

EQE spectra were acquired using the QuantX-300 (Newport). A monochromatic white xenon lamp (400 W) chopped at a frequency of 220 Hz was illuminated at the DUT, and the measured photocurrent was recorded with the wavelength of the incident light. The EQE spectrum was utilized to calculate the responsivity (R) of a photodetector through Eq. (1).

Noise and Detectivity Characterization

The noise current was measured by connecting the DUT to an SR570 low-noise current preamplifier and an SR830 lock-in amplifier for characterizing noise current at the wanted frequency. The overall measurements were conducted at 298 K under dark conditions. The noise current (I_N) was calculated from the noise voltage (V_N) and sensitivity of the LNA (S), and the specific detectivity (D^*) is derived from the Eq. (2).

Transient Photoresponse Characterization

The transient response of the photodiodes was characterized by recording the time-dependent photocurrent measured with a 500 MHz oscilloscope (DSO7054A, Tektronix), and a 1550 nm nanosecond pulsed laser (VFLS-1550-M-PL) with a 10 kHz repetition rate was used for the illumination.

Solution-Phase Ligand Exchange

Solution-phase ligand exchange was conducted based on a previous method with slight modifications [27]. We prepared a precursor solution by dissolving 0.2 mol of lead iodide (PbI$_2$), 0.04 mol of lead bromide (PbBr$_2$), and 0.08 mol of sodium acetate (NaOAc) in 20 mL of N,N-dimethylformamide (DMF) in a 50 mL conical tube. We added the 5.5 mg/mL oleic acid-capped PbS CQD solution to 10 mL of precursor solution. And we shake the mixture vigorously for 30 s to facilitate phase transfer. After the ligand exchange phase, the solution was washed with octane three times. After the wash step, toluene was added to the DMF solution to precipitate the exchanged PbS CQDs. And the precipitate CQDs were dried for 30 min under vacuum conditions. The CQDs were

redispersed in a 3:1 butylamine:DMF mixture at a concentration of 250 mg/mL.

Solar Cell Characterization

We measured the J–V characteristic of a solar cell by with a Keithley 2401 source meter. A Class AAA solar simulator from McScience Inc. was used for generating 1.5 AM solar light illumination. The QuantX-300 spectral measurement system is utilized to measure the monochromic photoresponse of the device.

Optical Simulation

The optical simulation is conducted using the transfer matrix method (TMM). The optical constants for material were obtained by the spectroscopic ellipsometry measurements (RC2, J,A, Woollam) and from previous research [66]. We calculated absorption by TMM from homemade MATLAB code [12, 14].

Data availability Data available on request from the authors.

Declarations

Conflict of interest The authors declare no competing interests.

References

1. S. Jee, M.J. Si, J.H. Choi, D. Kim, C. Kim, D. Yang, S.W. Baek, P-type colloidal InSb quantum dot ink enables III–V group bulk-heterojunction shortwave infrared (SWIR) photodetector. Adv. Opt. Mater. **12**, 2303097 (2024)
2. M. Biondi, M.J. Choi, Z. Wang, M. Wei, S. Lee, H. Choubisa, L.K. Sagar, B. Sun, S.W. Baek, B. Chen, Facet-oriented coupling enables fast and sensitive colloidal quantum dot photodetectors. Adv. Mater. **33**, 2101056 (2021)
3. D. Kim, G. Cho, Y.H. Kim, J.H. Kwon, Y. Oh, M. Yang, S. Jee, I.S. Lee, M.J. Si, Y. Jung, Multi-facet passivation of ternary colloidal quantum dot enabled by quadruple-ligand ensemble toward efficient lead-free optoelectronics. Adv. Energy Mater. **14**, 2302579 (2024)
4. J. Ko, B.G. Jeong, J.H. Chang, J.F. Joung, S.-Y. Yoon, D.C. Lee, S. Park, J. Huh, H. Yang, W.K. Bae, Chemically resistant and thermally stable quantum dots prepared by shell encapsulation with cross-linkable block copolymer ligands. NPG Asia Mater. **12**, 19 (2020)

5. H. Lee, D.-E. Yoon, S. Koh, M.S. Kang, J. Lim, D.C. Lee, Ligands as a universal molecular toolkit in synthesis and assembly of semiconductor nanocrystals. Chem. Sci. **11**, 2318 (2020)

6. Y.H. Kim, S. Koh, H. Lee, S.-M. Kang, D.C. Lee, B.-S. Bae, Photo-patternable quantum dots/siloxane composite with long-term stability for quantum dot color filters. ACS Appl. Mater. Interfaces **12**, 3961 (2019)

7. B. Sun, A.M. Najarian, L.K. Sagar, M. Biondi, M.J. Choi, X. Li, L. Levina, S.W. Baek, C. Zheng, S. Lee, Fast near-infrared photodetection using III–V colloidal quantum dots. Adv. Mater. **34**, 2203039 (2022)

8. S.H. Kim, D. Lee, S. Moon, J.H. Choi, D. Kim, J. Kim, S.W. Baek, Sulfurized colloidal quantum dot/tungsten disulfide multi-dimensional heterojunction for an efficient self-powered visible-to-SWIR photodetector. Adv. Funct. Mater.Funct. Mater. **33**, 2303778 (2023)

9. J.-H. Choi, M.-J. Si, S.-H. Kim, N. Maniyamgama, D. Kim, S. Jee, Y.H. Kim, H.-S. Jeong, B. Kim, C. Kim, Surface tailoring enables colloidal quantum dot: metal-oxide nanocrystal hybrid ink for broadband photon energy conversion. Appl. Surf. Sci. **612**, 155804 (2023)

10. M.J. Si, S. Jee, M. Yang, D. Kim, Y. Ahn, S. Lee, C. Kim, I.H. Bae, S.W. Baek, Colloidal InAs quantum dot-based infrared optoelectronics enabled by universal dual-ligand passivation. Adv. Sci. **11**, 2306798 (2024)

11. J.H. Kim, J.Y. Lee, J. Lim, J. Roh, S.W. Baek, W. Kim, M.C. Suh, H. Yu, Highly efficient top-emitting infrared-to-visible up-conversion device enabled by microcavity effect. Adv. Funct. Mater.Funct. Mater. **33**, 2214530 (2023)

12. J. Kim, D. Kim, W. Kim, S. Woo, S.-W. Baek, M.J. Ko, Y. Kim, Efficient semi-transparent perovskite quantum dot photovoltaics enabled by asymmetric dielectric/metal/dielectric transparent electrodes. Chem. Eng. J. **469**, 143824 (2023)

13. H. Opoku, Y.H. Kim, H. Lee, H. Ahn, J.-J. Lee, S.-W. Baek, J.W. Jo, A tailored graft-type polymer as a dopant-free hole transport material in indoor perovskite photovoltaics. J. Mater. Chem. A **9**, 15294 (2021)

14. J.H. Lee, D. Kim, H. Opoku, H. Ahn, J.-J. Lee, S.-W. Baek, J.W. Jo, Ethylene glycol-containing ammonium salt for developing highly compatible interfaces in perovskite solar cells. Chem. Eng. J. **455**, 140833 (2023)

15. S. Han, J. Kim, D.E. Kim, M.J. Ko, J. Choi, S.-W. Baek, Y. Kim, A small-molecule-templated nanostructure back electrode for enhanced light absorption and photocurrent in perovskite quantum dot photovoltaics. J. Mater. Chem. A **10**, 8966 (2022)

16. B. Kim, S.-W. Baek, C. Kim, J. Kim, J.-Y. Lee, Mediating colloidal quantum dot/organic semiconductor interfaces for efficient hybrid solar cells. Adv. Energy Mater. **12**, 2102689 (2022)

17. Y. Jung, H. Shin, S.-W. Baek, T.B. Tai, B. Scheffel, O. Ouellette, M. Biondi, S. Hoogland, F.P. GarcíadeArquer, E.H. Sargent, Near-unity broadband quantum efficiency enabled by colloidal quantum dot/mixed-organic heterojunction. ACS Energy Lett. **8**, 2331 (2023)

18. P. Sun, Z. Xing, Z. Li, W. Zhou, Recent advances in quantum dots photocatalysts. Chem. Eng. J. **458**, 141399 (2023)

19. J. Vargas, S. Alsweiss, O. Toker, R. Razdan, J. Santos, An overview of autonomous vehicles sensors and their vulnerability to weather conditions. Sensors **21**, 5397 (2021)

20. M. Vafaie, J.Z. Fan, A. MortezaNajarian, O. Ouellette, L.K. Sagar, K. Bertens, B. Sun, F.P. GarcíadeArquer, E.H. Sargent, Colloidal quantum dot photodetectors with 10-ns response time and 80% quantum efficiency at 1550 nm. Matter **4**, 1042 (2021)

21. A. Manekkathodi, B. Chen, J. Kim, S.-W. Baek, B. Scheffel, Y. Hou, O. Ouellette, M.I. Saidaminov, O. Voznyy, V.E. Madhavan, Solution-processed perovskite-colloidal quantum dot tandem solar cells for photon collection beyond 1000 nm. J. Mater. Chem. A **7**, 26020 (2019)

22. B. Chen, S.-W. Baek, Y. Hou, E. Aydin, M. De Bastiani, B. Scheffel, A. Proppe, Z. Huang, M. Wei, Y.-K. Wang, Enhanced optical path and electron diffusion length enable high-efficiency perovskite tandems. Nat. Commun.Commun. **11**, 1257 (2020)

23. M. Li, J. Yan, X. Zhao, T. Ma, A. Zhang, S. Chen, G. Shen, G.M.G. Khalaf, J. Zhang, C. Chen, Synergistic enhancement of efficient perovskite/quantum dot tandem solar cells based on transparent electrode and band alignment engineering. Adv. Energy Mater. **14**, 2400219 (2024)

24. R. Wang, Y. Shang, P. Kanjanaboos, W. Zhou, Z. Ning, E.H. Sargent, Colloidal quantum dot ligand engineering for high performance solar cells. Energy Environ. Sci. **9**, 1130 (2016)

25. M.-J. Choi, S.-W. Baek, S. Lee, M. Biondi, C. Zheng, P. Todorovic, P. Li, S. Hoogland, Z.-H. Lu, F.P.G. de Arquer, E.H. Sargent, Colloidal quantum dot bulk heterojunction solids with near-unity charge extraction efficiency. Adv. Sci. **7**, 2000894 (2020)

26. J.W. Jo, J. Choi, F.P. García de Arquer, A. Seifitokaldani, B. Sun, Y. Kim, H. Ahn, J. Fan, R. Quintero-Bermudez, J. Kim, Acid-assisted ligand exchange enhances coupling in colloidal quantum dot solids. Nano Lett. **18**, 4417 (2018)

27. J.Z. Fan, M. Vafaie, K. Bertens, M. Sytnyk, J.M. Pina, L.K. Sagar, O. Ouellette, A.H. Proppe, A.S. Rasouli, Y. Gao, Micron thick colloidal quantum dot solids. Nano Lett. **20**, 5284 (2020)

28. O.T. Bruns, T.S. Bischof, D.K. Harris, D. Franke, Y. Shi, L. Riedemann, A. Bartelt, F.B. Jaworski, J.A. Carr, C.J. Rowlands, M.W.B. Wilson, O. Chen, H. Wei, G.W. Hwang, D.M. Montana, I. Coropceanu, O.B. Achorn, J. Kloepper, J. Heeren, P.T.C. So, D. Fukumura, K.F. Jensen, R.K. Jain, M.G. Bawendi, Next-generation in vivo optical imaging with short-wave infrared quantum dots. Nat. Biomed. Eng. **1**, 0056 (2017)

29. C. Blanch-Perez-Del-Notario, S. Thijs, M. Jayapala, Band relevance study of SWIR hyperspectral imaging for material recycling and reuse, in *2023 13th Workshop on Hyperspectral Imaging and Signal Processing: Evolution in Remote Sensing (WHISPERS)* (2023), pp. 1–5

30. R. Tobin, A. Halimi, A. McCarthy, P.J. Soan, G.S. Buller, Robust real-time 3D imaging of moving scenes through atmospheric obscurant using single-photon LiDAR. Sci. Rep. **11**, 11236 (2021)

31. M.A. Hines, G.D. Scholes, Colloidal PbS nanocrystals with size-tunable near-infrared emission: observation of post-synthesis self-narrowing of the particle size distribution. Adv. Mater. **15**, 1844 (2003)

32. H. Lee, D.-H. Cho, C. Lim, W. Kim, Y.H. Jang, S.-W. Baek, B.K. Ju, P. Lee, H. Yu, Pressurized back-junction doping via spray-coating silver nanowires top electrodes for efficient charge collection in bifacial colloidal PbS quantum dot solar cells. ACS Appl. Mater. Interfaces **16**, 7130 (2024)

33 E.H. Sargent, Infrared quantum dots. Adv. Mater. **17**, 515 (2005)

34. S. Lee, D.T. Lee, J.-H. Ko, W.-J. Kim, J. Joo, S. Jeong, J.A. McGuire, Y.-H. Kim, D.C. Lee, Slow colloidal growth of PbSe nanocrystals for facile morphology and size control. RSC Adv. **4**, 9842 (2014)

35. D. Kim, Y.K. Lee, D. Lee, W.D. Kim, W.K. Bae, D.C. Lee, Colloidal dual-diameter and core-position-controlled core/shell cadmium chalcogenide nanorods. ACS Nano **11**, 12461 (2017)

36. H. Yun, Y.J. Lee, M. Xu, D.C. Lee, G.E. Stein, B.J. Kim, Softness-and size-dependent packing symmetries of polymer-grafted nanoparticles. ACS Nano **14**, 9644 (2020)

37. J. Zhang, J. Gao, E.M. Miller, J.M. Luther, M.C. Beard, Diffusion-controlled synthesis of PbS and PbSe quantum dots with in situ halide passivation for quantum dot solar cells. ACS Nano **8**, 614 (2014)

38. S. Abe, R.K. Capek, B. De Geyter, Z. Hens, Reaction chemistry/nanocrystal property relations in the hot injection synthesis, the role of the solute solubility. ACS Nano **7**, 943 (2013)

39. J. Zhang, R.W. Crisp, J. Gao, D.M. Kroupa, M.C. Beard, J.M. Luther, Synthetic conditions for high-accuracy size control of PbS quantum dots. J. Phys. Chem. Lett. **6**, 1830 (2015)

40. L. Cademartiri, J. Bertolotti, R. Sapienza, D.S. Wiersma, G. Von Freymann, G.A. Ozin, Multigram scale, solventless, and diffusion-controlled route to highly monodisperse PbS nanocrystals. J. Phys. Chem. B **110**, 671 (2006)

41. D.V. Talapin, A.L. Rogach, M. Haase, H. Weller, Evolution of an ensemble of nanoparticles in a colloidal solution: theoretical study. J. Phys. Chem. B **105**, 12278 (2001)

42. I. Moreels, Y. Justo, B. De Geyter, K. Haustraete, J.C. Martins, Z. Hens, Size-tunable, bright, and stable PbS quantum dots: a surface chemistry study. ACS Nano **5**, 2004 (2011)

43. H. Wang, J. Pinna, D.G. Romero, L. Di Mario, R.M. Koushki, M. Kot, G. Portale, M.A. Loi, PbS quantum dots ink with months-long shelf-lifetime enabling scalable and efficient short-wavelength infrared photodetectors. Adv. Mater. **36**, 2311526 (2024)

44. M.I. Nugraha, H. Kim, B. Sun, M.A. Haque, F.P.G. de Arquer, D.R. Villalva, A. El-Labban, E.H. Sargent, H.N. Alshareef, D. Baran, Low-temperature-processed colloidal quantum dots as building blocks for thermoelectrics. Adv. Energy Mater. **9**, 1803049 (2019)

45. M. Gu, Y. Wang, F. Yang, K. Lu, Y. Xue, T. Wu, H. Fang, S. Zhou, Y. Zhang, X. Ling, Y. Xu, F. Li, J. Yuan, M.A. Loi, Z. Liu, W. Ma, Stable PbS quantum dot ink for efficient solar cells by solution-phase ligand engineering. J. Mater. Chem. A **7**, 15951 (2019)

46. H.R. You, J.Y. Park, D.H. Lee, Y. Kim, J. Choi, Recent research progress in surface ligand exchange of PbS quantum dots for solar cell application. Appl. Sci. **10**, 975 (2020)

47. A. Fischer, L. Rollny, J. Pan, G.H. Carey, S.M. Thon, S. Hoogland, O. Voznyy, D. Zhitomirsky, J.Y. Kim, O.M. Bakr, E.H. Sargent, Directly deposited quantum dot solids using a colloidally stable nanoparticle ink. Adv. Mater. **25**, 5742 (2013)

48. F. Yang, D.-W. Kang, Y.-S. Kim, Improved interface of ZnO/CH3NH3PbI3 by a dynamic spin-coating process for efficient perovskite solar cells. RSC Adv. **7**, 19030 (2017)

49. M.-J. Choi, L.K. Sagar, B. Sun, M. Biondi, S. Lee, A.M. Najjariyan, L. Levina, F.P. García de Arquer, E.H. Sargent, Ligand exchange at a covalent surface enables balanced stoichiometry in III–V colloidal quantum dots. Nano Lett. **21**, 6057 (2021)

50. N. Sukharevska, D. Bederak, V.M. Goossens, J. Momand, H. Duim, D.N. Dirin, M.V. Kovalenko, B.J. Kooi, M.A. Loi, Scalable PbS quantum dot solar cell production by blade coating from stable inks. ACS Appl. Mater. Interfaces **13**, 5195 (2021)

51. D. Chen, Y. Liu, B. Xia, L. Chen, Y. Yang, G. Yang, J. Liu, S. Lu, C. Ge, P. Liu, J. Yang, G. Liang, X. Lan, X. Zeng, L. Li, J. Zhang, Z. Xiao, L. Gao, J. Tang, Passivating 100 facets of PbS colloidal quantum dots via perovskite bridges for sensitive and stable infrared photodiodes. Adv. Funct. Mater.Funct. Mater. **33**, 2210158 (2023)

52. J.Z. Fan, N.T. Andersen, M. Biondi, P. Todorović, B. Sun, O. Ouellette, J. Abed, L.K. Sagar, M.-J. Choi, S. Hoogland, F.P.G. de Arquer, E.H. Sargent, Mixed lead halide passivation of quantum dots. Adv. Mater. **31**, 1904304 (2019)

53. P. Liu, S. Lu, J. Liu, B. Xia, G. Yang, M. Ke, X. Zhao, J. Yang, Y. Liu, C. Ge, G. Liang, W. Chen, X. Lan, J. Zhang, L. Gao, J. Tang, Double-ended passivator enables dark-current-suppressed colloidal quantum dot photodiodes for CMOS-integrated infrared imagers. InfoMat **6**, e12497 (2024)

54. J. Han, D. Yang, D. Ma, W. Qiao, Z.Y. Wang, Low-bandgap polymers for high-performance photodiodes with maximal EQE near 1200 nm and broad spectral response from 300 to 1700 nm. Adv. Opt. Mat. **6**, 1800038 (2018)

55. M. Liu, O. Voznyy, R. Sabatini, F.P. García de Arquer, R. Munir, A.H. Balawi, X. Lan, F. Fan, G. Walters, A.R. Kirmani, S. Hoogland, F. Laquai, A. Amassian, E.H. Sargent, Hybrid organic–inorganic inks flatten the energy landscape in colloidal quantum dot solids. Nat. Mater. **16**, 258 (2017)

56. S. Lee, M.-J. Choi, G. Sharma, M. Biondi, B. Chen, S.-W. Baek, A.M. Najarian, M. Vafaie, J. Wicks, L.K. Sagar, S. Hoogland, F.P.G. de Arquer, O. Voznyy, E.H. Sargent, Orthogonal colloidal quantum dot inks enable efficient multilayer optoelectronic devices. Nat. Commun.Commun. **11**, 4814 (2020)

57. J. Kublitski, A. Hofacker, B.K. Boroujeni, J. Benduhn, V.C. Nikolis, C. Kaiser, D. Spoltore, H. Kleemann, A. Fischer, F. Ellinger, K. Vandewal, K. Leo, Reverse dark current in organic photodetectors and the major role of traps as source of noise. Nat. Commun. Commun. **12**, 551 (2021)

58. B.G. Akinoglu, B. Tuncel, V. Badescu, Beyond 3rd generation solar cells and the full spectrum project. Recent advances and new emerging solar cells. Sustain. Energy Technol. Assess. **46**, 101287 (2021)

59. Y.H. Lee, *Beyond the Shockley–Queisser Limit: Exploring New Frontiers in Solar Energy Harvest* (American Association for the Advancement of Science, 2024), p. eado4308

60. W. Shockley, H. Queisser, Detailed balance limit of efficiency of pn junction solar cells. J. Appl. Phys. **32**, 510 (1961)

61. A. Karani, L. Yang, S. Bai, M.H. Futscher, H.J. Snaith, B. Ehrler, N.C. Greenham, D. Di, Perovskite/colloidal quantum dot tandem solar cells: theoretical modeling and monolithic structure. ACS Energy Lett. **3**, 869 (2018)

62. S. Gharibzadeh, I.M. Hossain, P. Fassl, B.A. Nejand, T. Abzieher, M. Schultes, E. Ahlswede, P. Jackson, M. Powalla, S. Schäfer, 2D/3D heterostructure for semitransparent perovskite solar cells with engineered bandgap enables efficiencies exceeding 25% in four-terminal tandems with silicon and cigs. Adv. Funct. Mater. Funct. Mater. **30**, 1909919 (2020)

63. W. Yang, H. Long, X. Sha, J. Sun, Y. Zhao, C. Guo, X. Peng, C. Shou, X. Yang, J. Sheng, Unlocking voltage potentials of mixed-halide perovskite solar cells via phase segregation suppression. Adv. Funct. Mater.Funct. Mater. **32**, 2110698 (2022)

64. J. Liu, K. Xian, L. Ye, Z. Zhou, Open-circuit voltage loss in lead chalcogenide quantum dot solar cells. Adv. Mater. **33**, 2008115 (2021)

65. H.-S. Jeong, D. Kim, S. Jee, M.-J. Si, C. Kim, J.-Y. Lee, Y. Jung, S.-W. Baek, Colloidal quantum dot: organic ternary ink for efficient solution-processed hybrid solar cells. Int. J. Energy Res. **2023**, 1–14 (2023)

66. B. Chehaibou, E. Izquierdo, A. Chu, C. Abadie, M. Cavallo, A. Khalili, T.H. Dang, C. Greboval, X.Z. Xu, S. Ithurria, The complex optical index of PbS nanocrystal thin films and their use for short wave infrared sensor design. Nanoscale **14**, 2711 (2022)